

# Inducing locally structured ion energy distributions in intermediate-pressure plasmas

Cite as: Phys. Plasmas **26**, 073519 (2019); <https://doi.org/10.1063/1.5111401>

Submitted: 25 May 2019 . Accepted: 08 July 2019 . Published Online: 31 July 2019

Scott J. Doyle , Andrew R. Gibson , Rod W. Boswell, Christine Charles, and James P. Dedrick 



View Online



Export Citation



CrossMark

## ARTICLES YOU MAY BE INTERESTED IN

### [Electron kinetics in low-temperature plasmas](#)

Physics of Plasmas **26**, 060601 (2019); <https://doi.org/10.1063/1.5093199>

### [Numerical solutions of Maxwell's equations in 3D in frequency domain with linear sheath boundary conditions](#)

Physics of Plasmas **26**, 083501 (2019); <https://doi.org/10.1063/1.5111500>

### [Mean force kinetic theory: A convergent kinetic theory for weakly and strongly coupled plasmas](#)

Physics of Plasmas **26**, 082106 (2019); <https://doi.org/10.1063/1.5095655>



**ULVAC**

**Leading the World with Vacuum Technology**

- Vacuum Pumps
- Arc Plasma Deposition
- RGAs
- Leak Detectors
- Thermal Analysis
- Ellipsometers

# Inducing locally structured ion energy distributions in intermediate-pressure plasmas

Cite as: Phys. Plasmas **26**, 073519 (2019); doi: 10.1063/1.5111401

Submitted: 25 May 2019 · Accepted: 8 July 2019 ·

Published Online: 31 July 2019






View Online



Export Citation



CrossMark

Scott J. Doyle,<sup>1,a)</sup>  Andrew R. Gibson,<sup>1,2,3</sup>  Rod W. Boswell,<sup>4</sup> Christine Charles,<sup>4</sup> and James P. Dedrick<sup>1</sup> 

## AFFILIATIONS

<sup>1</sup>Department of Physics, York Plasma Institute, University of York, Heslington, York YO10 5DD, United Kingdom

<sup>2</sup>Research Group for Biomedical Plasma Technology, Ruhr-Universität Bochum, Universitätsstraße 150, 44801 Bochum, Germany

<sup>3</sup>Institute of Electrical Engineering and Plasma Technology, Ruhr-Universität Bochum, Universitätsstraße 150, 44801 Bochum, Germany

<sup>4</sup>Space Plasma, Power and Propulsion Laboratory, Research School of Physics and Engineering, The Australian National University, Canberra, ACT 2601, Australia

<sup>a)</sup>Electronic mail: [Scott.Doyle@Physics.org](mailto:Scott.Doyle@Physics.org)

## ABSTRACT

Ion energy distribution functions (IEDFs) incident upon material surfaces in radio frequency (rf) capacitively coupled plasmas are coupled to spatial and temporal sheath dynamics. Tailoring the ion energy distribution function within intermediate-pressure plasmas ( $\approx 133$  Pa, 1 Torr), which find application in surface modification and aerospace industries, is challenging due to the collisional conditions. In this work, experimentally benchmarked 2D fluid/Monte-Carlo simulations are employed to demonstrate the production of structured IEDFs in a collisional (200 Pa 1.5 Torr argon) rf hollow cathode discharge. The formation of structures within the IEDFs is explained by an increase in the  $\text{Ar}^+$  ion-neutral mean-free-path and a simultaneous decrease in the phase-averaged sheath extension as the rf voltage frequency increases over 13.56–108.48 MHz for a constant rf voltage amplitude (increasing plasma power) and gas flow rate. Two distinct transitions in the shape of the IEDF are observed at 450 V, corresponding to the formation of “mid-energy” (60–180 eV) structures between 40.68 and 54.24 MHz and additional “high energy” ( $\geq 180$  eV) structures between 81.36 and 94.92 MHz, with the structures within each region displaying a distinct sensitivity to the applied voltage amplitude. Transitions between these energy ranges occurred at lower applied voltages for increased applied voltage frequencies, providing increased control of the mean and modal ion energy over a wider voltage range. The capability to extend the range of access to an operational regime, where the structured IEDFs are observed, is desirable for applications that require control of the ion-bombardment energy under collisional plasma conditions.

Published under license by AIP Publishing. <https://doi.org/10.1063/1.5111401>

## I. INTRODUCTION

The enhancement of capacitively coupled plasma (CCP) sources through the implementation of hollow cathode (HC) geometries represents an area of recent interest.<sup>1–4</sup> Applications of HC sources range from scalable arrays for homogeneous surface modification<sup>5,6</sup> to microdischarge sources for spacecraft propulsion.<sup>7–9</sup> Control of the ion energy distribution function (IEDF) throughout the plasma has been found to be important for these applications.<sup>1,10</sup> For example, in the semiconductor industry, the IEDF incident upon material surfaces plays a crucial role in the quality and homogeneity of etching and deposition processes.<sup>6,11</sup> Ions that are accelerated through sheaths adjacent to plasma facing surfaces impact the wall with an energy distribution that is dependent upon the ion-neutral collision frequencies, the phase-averaged sheath width, and the sheath potential.<sup>12</sup> The

resulting mean and modal ion-bombardment energies can therefore be significantly affected by the amplitude and frequency of the applied voltage waveform.<sup>13</sup>

Structured IEDFs differ from unstructured distributions as they exhibit additional characteristic peaks, typically associated with the radio frequency modulation of the sheath potential.<sup>14</sup> Previous works related to structured IEDFs in rf plasmas were primarily focused over the range from low to intermediate pressure discharges (0.65–67 Pa, 5–500 mTorr) at applied voltage frequencies of 13.56 MHz<sup>14–17</sup> and 27.12 MHz.<sup>18</sup> More recent work has demonstrated the control of the IEDF in low-pressure (0.65–1.3 Pa, 5–10 mTorr) plasmas through the application of higher applied voltage frequencies in the range of 12 MHz–100 MHz.<sup>12,19,20</sup> For applications involving higher-pressure discharges (above 200 Pa, 1.5 Torr), the increased ion-neutral collision

frequency results in a collisionally dominated IEDF at the wall, the shape of which is largely independent of the voltage amplitude, limiting the range of accessible ion energies.<sup>12</sup> At these pressures, heating and rarefaction of the neutral gas play a substantial role in determining the heavy particle collision rates and mean-free-paths.<sup>21,22</sup> Therefore, to adequately model the IEDF at these pressures, it is necessary to self-consistently solve for the change in neutral gas density that mediates the transfer of energy through ion-neutral collisions.

In this work, the formation of structured IEDFs with increasing driving frequency (13.56–108.48 MHz) in a collisional (200 Pa, 1.5 Torr argon) capacitively coupled hollow-cathode microdischarge is investigated through the application of an experimentally validated two-dimensional fluid/Monte-Carlo model. A brief description of the experimental setup and numerical model is given in Sec. II. Agreement between the measured and simulated  $\text{Ar}(2p_1-1s_2)$  electron impact excitation rates is demonstrated for applied voltage frequencies of 13.56 MHz, 27.12 MHz, and 40.68 MHz at an applied voltage of 450 V in Sec. III. Additional simulations are employed to draw conclusions up to 108.48 MHz, where the evolution of the IEDFs with respect to the applied voltage amplitude and frequency is presented in Sec. IV. The corresponding variation in the  $\text{Ar}^+$  mean-free-path and radial sheath extension, and how these drive the formation of the structured IEDFs, is discussed in Sec. V.

## II. EXPERIMENTAL METHOD AND SIMULATION MODEL

The hollow cathode microdischarge source, shown in Fig. 1, employs an annular powered electrode surrounding a 4.2 mm inner-diameter alumina tube through which 100 sccm of argon gas is supplied.<sup>23–29</sup> During steady-state operation, an axial pressure gradient exists between the plenum at 200 Pa (1.5 Torr) and the expansion region at 113 Pa (0.85 Torr).

In the experiment, power is supplied via an arbitrary waveform generator (Keysight 33621A, 120 MHz), broadband amplifier (IFI

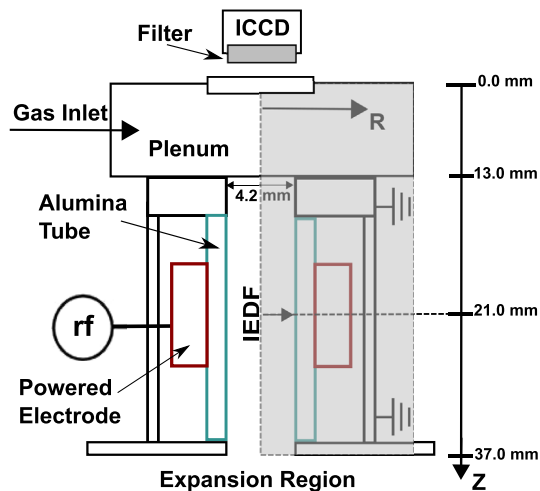


**FIG. 1.** Schematic of the experimental setup (not to scale), where the simulated region is denoted by the shaded gray area. The imaging plane of the ICCD camera is centered on the midplane of the powered electrode ( $Z = 21$  mm). Simulated IEDFs are obtained from  $\text{Ar}^+$  ions incident on the radial wall ( $R, Z = 2.1$  mm, 21 mm) as denoted by the solid arrow.

SCCX100, 0.01–220 MHz), and matching network connected in series with the powered electrode. The grounded electrode area in contact with the plasma exceeds the powered electrode area. Therefore, to maintain current continuity through both the powered and grounded surfaces, a dc self-bias voltage forms on the surface of the alumina wall adjacent to the powered electrode.<sup>30,31</sup> Argon ions are accelerated radially through the sheath adjacent to the powered electrode and undergo ion-neutral charge exchange collisions, resulting in significant neutral gas heating within the powered electrode sheath.<sup>21,22,25,32</sup> Secondary electrons, released through positive ion bombardment, are accelerated back into the plasma bulk at high, nonthermal energies (above 50 eV), representing an efficient additional ionization mechanism.<sup>33,34</sup>

Two-dimensional, fluid-kinetic simulations were performed using the Hybrid Plasma Equipment Model (HPEM).<sup>35</sup> A full description of the mesh and numerical methods applied can be found in Refs. 22 and 36; a summary is provided here. The simulated region is shown in Fig. 1 as the shaded gray area. The simulation mesh consisted of a rectilinear grid of  $64 \times 152$  ( $R \times Z$ ) cells in a cylindrically symmetric geometry, corresponding to a radial resolution of 0.125 mm per cell and an axial resolution of 0.5 mm per cell. A higher radial resolution was employed to enable a discussion of the phase-resolved sheath dynamics perpendicular to the dielectric surface. The sheath extension is calculated as in Ref. 36, where the radial sheath edge  $S_R$  is determined as the radius  $R$  that satisfies the Brinkmann criterion.<sup>37</sup>

Species considered within the model are Ar,  $\text{Ar}(4s)$ ,  $\text{Ar}(4p)$ ,  $\text{Ar}(4d)$ ,  $\text{Ar}_2^+$ ,  $\text{Ar}^+$ ,  $\text{Ar}_2^+$ , and  $e^-$ , where the reaction mechanism is as discussed in Ref. 38. Gas-phase electron-neutral and electron-ion collisions include elastic, excitation, and ionization reactions.<sup>38</sup> Cascade processes, multistep ionization, and heavy particle mixing between excited species are also included, the interaction cross sections for which are obtained from Refs. 39–43. Ion-neutral charge exchange collisions are employed with a rate coefficient of  $5.66 \times 10^{-10} \text{ cm}^3 \text{ s}^{-1} (T_g/300)^{0.5}$ , where  $T_g$  is the neutral-gas temperature.<sup>44</sup> The energy distribution functions for all gas-phase heavy particle species are assumed to be Maxwellian and are obtained from a two-term approximation of the Boltzmann equation. Ion energy distributions for  $\text{Ar}^+$  incident on the radial wall at ( $R, Z = 2.1$  mm, 21 mm) are obtained via a kinetic Monte-Carlo algorithm by employing the same reaction mechanism as used in the gas phase.<sup>35</sup>

Phase-resolved optical emission spectroscopy (PROES)<sup>45,46</sup> was performed to enable a comparison of the measured and simulated electron heating mechanisms and hence also the phase-resolved sheath dynamics. For further details, see Ref. 22. Images were acquired using an intensified charge coupled device (ICCD) camera (Andor iStar DH344T-18U-73,  $1024 \times 1024$  array, pixel size:  $13 \times 13 \mu\text{m}^2$ ) by employing an optical gate width of 1.7 ns and a 750.466 nm bandpass filter (LOT-QuantumDesign, 1 nm FWHM). A depth of field of 24 mm, corresponding to the axial length of the source region, was applied to the simulated PROES images through a top hat integration along the line of sight.<sup>47</sup> Previous work has demonstrated agreement between the measured and simulated phase-resolved,  $\text{Ar}(2p_1)$  electron impact excitation rates in this source.<sup>22,36</sup> Here, experimental comparisons are presented for 13.56 MHz, 27.12 MHz, and 40.68 MHz applied voltage frequencies at an applied voltage amplitude of  $\phi_{\text{rf}} = 450$  V. Additional simulations are employed to draw conclusions up to 108.48 MHz.

### III. ELECTRON-IMPACT EXCITATION RATE: SIMULATIONS AND EXPERIMENTS

The measured and simulated  $\text{Ar}(2p_1)$  excitation rates for driving frequency discharges of 13.56 MHz, 27.12 MHz, and 40.68 MHz at an applied voltage amplitude of 450 V are shown in Fig. 2.

At 13.56 MHz [Figs. 2(a) and 2(d)], close agreement is observed between simulation and experiment and a similarly high level of agreement is observed over a wider voltage range of 150–450 V (not shown), representing the full operational range of the experiment. Here, peak A represents electron heating due to the collapsing sheath edge,<sup>48</sup> while peak C represents secondary electron impact excitation<sup>49</sup> in the phase of most negative dielectric surface potential,  $\tau = 0.75$ .

Similar spatiotemporal heating mechanisms are observed for 27.12 MHz, shown in Figs. 2(b) and 2(e). Secondary electron excitation (peak C) remains the dominant electron heating mechanism in both the measurement and the simulation. Sheath expansion heating<sup>50</sup> (peak B) is observed in both simulation and experiment over the phase interval of  $0.4 \leq \tau \leq 0.7$ . Although close agreement is observed between simulation and experiment at 27.12 MHz for peaks B and C, sheath collapse heating (peak A) is overestimated in the simulation. The degree of excitation during sheath collapse is proportional to the mean electron velocity out of the plasma bulk, where the total electron flux during the phase of sheath collapse must balance the positive ion loss during phases where the sheath extent is greater than zero.<sup>30</sup> For a given electron-neutral collision frequency, a reduction in the electron density will enforce an increase in the average electron velocity to maintain the same flux. Therefore, the overestimation in sheath collapse heating may indicate an underestimated plasma density in the simulation as compared to the experiment.<sup>51,52</sup>

As the driving frequency is increased to 40.68 MHz, the dominant electron heating mechanism shifts from secondary electron heating (peak C) to sheath expansion heating (peak B), shown in Figs. 2(c) and 2(f). This transition occurs as sheath expansion heating is dependent upon the expanding sheath velocity, which increases with increasing driving frequency. In contrast, the reduction in the secondary electron excitation arises from a reduction in the absolute time for which the sheath is fully extended. Sheath collapse heating (peak A) remains overestimated through the same reasoning as for 27.12 MHz. Sheath expansion heating and heating via secondary electrons are less sensitive to changes in the plasma density as they are to variations in the sheath dynamics.<sup>48</sup> Therefore, as close agreement is observed between simulation and experiment with respect to sheath expansion and secondary electron heating and their transition at 40.68 MHz, it may be inferred that the phase-resolved sheath dynamics are being modeled appropriately. Note that an underestimation of the  $\text{Ar}^+$  ion density will likely result in a slight systematic overestimation of the sheath extent.<sup>31</sup>

### IV. EVOLUTION OF ION ENERGY DISTRIBUTION FUNCTIONS

Figure 3 shows the evolution of the  $\text{Ar}^+$  IEDFs incident on the alumina wall adjacent to the powered electrode ( $R, Z = 2.1$  mm, 21 mm) with respect to applied voltage for 13.56–108.48 MHz over the voltage range of 150–450 V.

In Fig. 3, the mean and the modal  $\hat{\epsilon}_{\text{Ar}^+}$  ion energies are denoted by the black and white lines, respectively. Here, the modal ion energy represents the most populous structure within the distribution, while the mean more generally characterizes the entire distribution. The 13.56 MHz IEDFs in Fig. 3(a) exhibit profiles where the majority of  $\text{Ar}^+$  ions are maintained at low energies ( $0.6 \text{ eV} \leq \hat{\epsilon}_{\text{Ar}^+} \leq 6 \text{ eV}$ ),

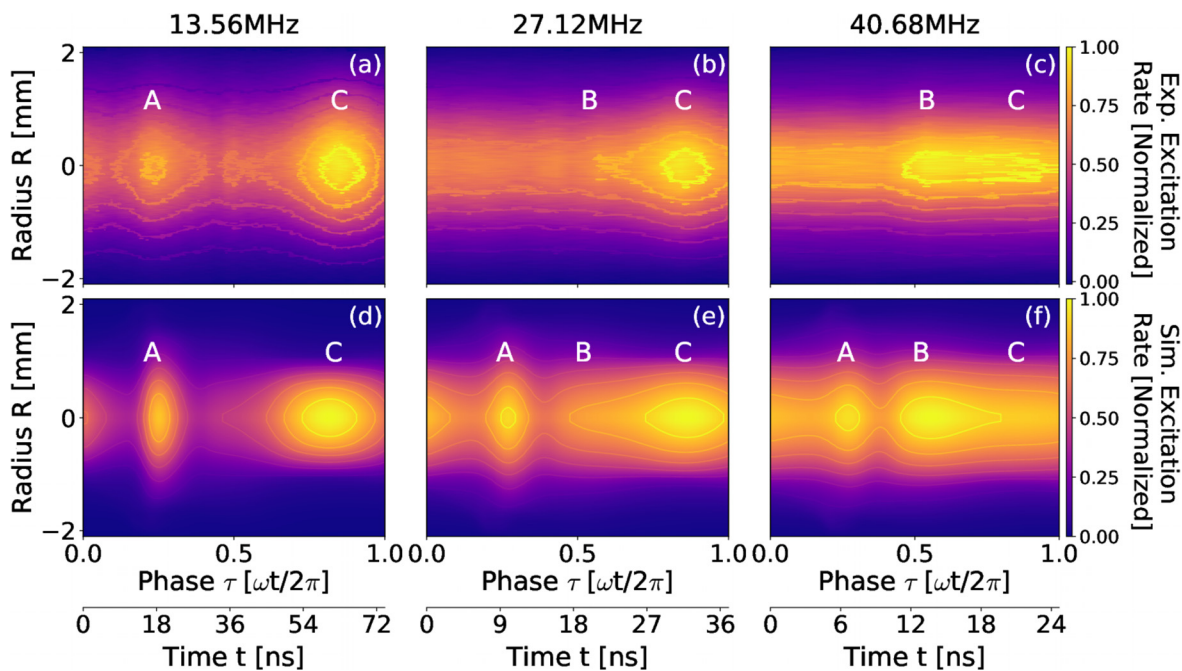
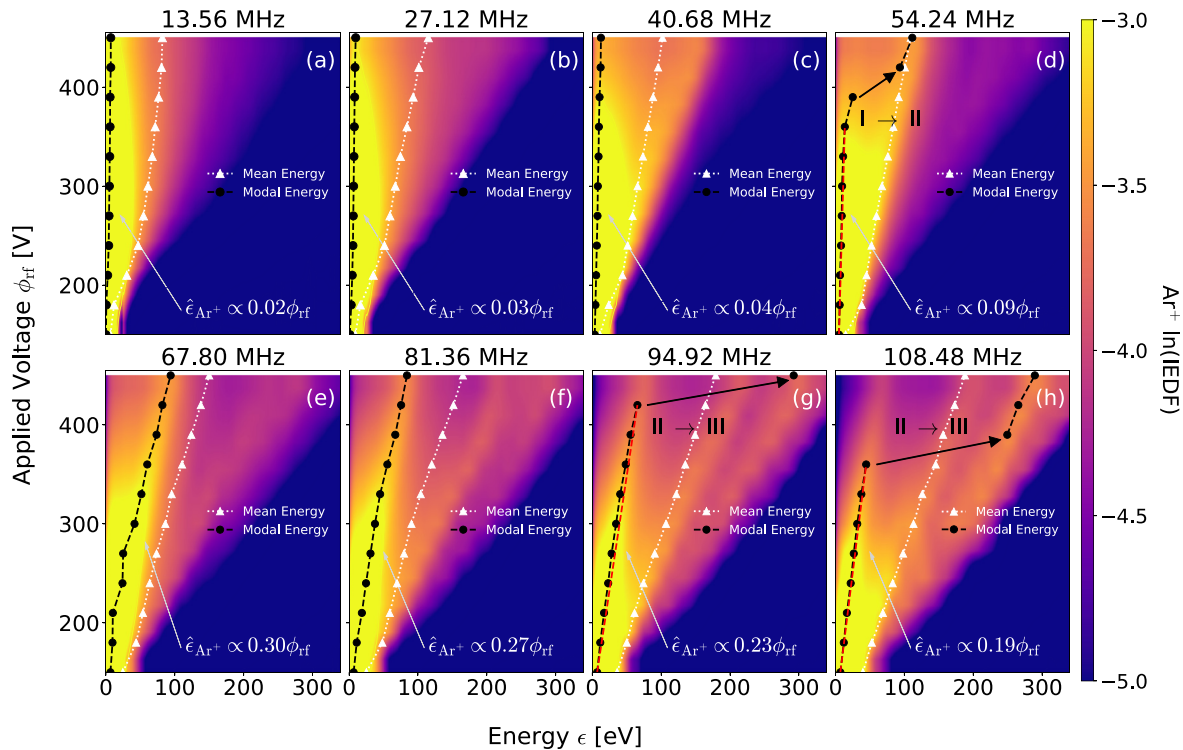


FIG. 2.  $\text{Ar}(2p_1)$  excitation rates for applied voltage frequencies of 13.56 MHz, 27.12 MHz, and 40.68 MHz as measured experimentally [(a)–(c)] and via simulation [(d)–(f)]. The plenum pressure is 200 Pa (1.5 Torr) argon; applied voltage  $\phi_{rf} = 450$  V.





**FIG. 3.**  $\text{Ar}^+$  ion energy distribution functions incident on the dielectric radial wall adjacent to the powered electrode ( $R, Z = 2.1$  mm, 21 mm, see Fig. 1), for applied voltage amplitudes of 150–450 V and applied voltage frequencies of 13.56–108.48 MHz (a)–(h). The mean and modal  $\hat{\epsilon}_{\text{Ar}^+}$  ion energies are indicated by dotted and dashed lines, respectively, where discontinuous transitions in the modal  $\text{Ar}^+$  energy are denoted by the black arrows in panels (d), (g), and (h). The modal energy proportionalities to the applied voltage are obtained from linear fits over the full voltage range, with the exception of 54.24 MHz, 94.92 MHz, and 108.48 MHz, which are performed over the voltage ranges of 150–360 V, 150–420 V, and 150–360 V, respectively, as denoted by the red dashed lines in the associated panels. The colourbar scale has been reduced, omitting IEDF fractions above  $10^{-3}$  and below  $10^{-5}$  for clarity. The plenum pressure is 200 Pa (1.5 Torr) argon;  $\phi_{\text{rf}} = 150$ –450 V.

supplemented by a high energy (50–200 eV) tail containing relatively few ions. This structure is expected for the relatively high pressure (200 Pa, 1.5 Torr) discharge conditions, where the ion-neutral collision frequency is high.<sup>10,12,53</sup> As a result, the mean and the modal ion energies exhibit little change with varying applied voltage amplitudes. Note, however, that an increase in the fraction of ions within the high energy tail is observed with the increasing applied voltage amplitude.

Increasing the driving frequency to 27.12 MHz, Fig. 3(b), results in much the same behavior as observed for the 13.56 MHz case. The first notable change in the shape of the IEDFs occurs between 40.68 MHz and 54.24 MHz, Figs. 3(c) and 3(d), respectively, where the IEDFs exhibit an additional mid-energy ( $\approx 60$ –180 eV) structure in addition to the low energy ( $\leq 60$  eV) structure observed previously. The modal ion energy transitions into this structure for applied voltage amplitudes above 390 V at 54.24 MHz, denoted by “I  $\rightarrow$  II” in Fig. 3(d), representing a distinct transition in the distribution of energies within the IEDF.

For applied voltage frequencies of 67.80 MHz and 81.36 MHz, Figs. 3(e) and 3(f), the modal ion energy sits within the mid-energy structure for almost the entire voltage range. This represents an increased sensitivity of the modal ion energy to the applied voltage amplitude. In addition, an increase in the fraction of ions within the high energy tail of the distribution ( $\approx 180$  eV) is observed. The high

energy tail begins to stratify into two further structures, positioned on either side of the mean energy of the distribution, for applied voltage frequencies of 94.92 MHz and 108.48 MHz in Figs. 3(g) and 3(h). Here, a structure refers to a subcomponent of the IEDF that can be best approximated via a Gaussian or Lorentzian distribution as opposed to a Maxwell-Boltzmann distribution. The fraction of ions within these structures increases in proportion to the applied voltage amplitude, until the modal ion energy exhibits a transition into the highest energy structure at 450 V for 94.92 MHz [“II  $\rightarrow$  III” in Fig. 3(g)]. This transition occurs at a lower voltage of 390 V for 108.48 MHz.

The trends observed in Figs. 3(a)–3(h) indicate the formation of mid-energy ( $\approx 60$ –180 eV) and high energy ( $\geq 180$  eV) structures (II and III, respectively) in the IEDFs, the formation and evolution of which vary with both the driving frequency and the amplitude. To further characterize these structures, the IEDFs incident on the alumina wall adjacent to the powered electrode ( $R, Z = 2.1$  mm, 21 mm), for varying applied voltage frequencies between 13.56 and 108.48 MHz at an applied voltage amplitude of 450 V, are shown in Fig. 4.

The structures within the IEDFs presented in Fig. 4 can be categorized into three energy ranges: Region I (0–60 eV) contains the largest fraction of ions for applied voltage frequencies between 13.56 and 40.68 MHz. This region consists primarily of low energy ions where the modal ion energy  $\hat{\epsilon}_{\text{Ar}^+}$  is far below the phase-averaged sheath

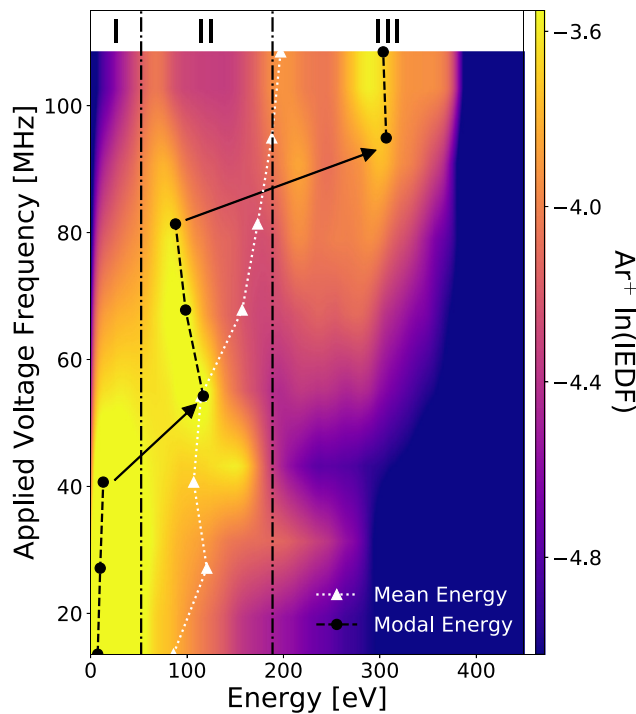


**FIG. 4.**  $\text{Ar}^+$  ion energy distribution functions incident on the dielectric radial wall adjacent to the powered electrode ( $R, Z = 2.1$  mm, 21 mm, see Fig. 1), for applied voltage frequencies between 13.56 and 108.48 MHz and an applied voltage amplitude of 450 V. The modal  $\hat{\epsilon}_{\text{Ar}^+}$  and mean  $\text{Ar}^+$  ion energies are denoted by the black dashed and white dotted lines, respectively. The IEDFs can be broadly described by structures in three energy regions, separated by the dashed-dotted lines, which correspond to I (0–60 eV), II (60–180 eV), and III ( $\geq 180$  eV). For clarity, the colourbar dynamic scale has been reduced, omitting IEDF fractions below  $10^{-5}$ . The plenum pressure is 200 Pa (1.5 Torr) argon, and the applied voltage amplitude is 450 V.

potential ( $\approx -350$  V), indicating a regime in which this is determined primarily through the high ion-neutral collision frequency. Region II (60–180 eV) contains the largest fraction of the IEDF for applied voltage frequencies between 54.24 and 81.36 MHz, and this structure becomes visible above 40.68 MHz. This region consists of a single mid-energy structure, the magnitude of which increases until approximately 67.80 MHz and decreases thereafter. The modal energy in this region is inversely proportional to the driving frequency, leveling off at  $\approx 80$  eV for frequencies above 94.92 MHz.

For applied voltage frequencies of 67.80–108.48 MHz, two additional high energy peaks begin to form in region III, above 180 eV. The formation of these structures is observed for applied voltage frequencies above 67.80 MHz as a single broadband (80 eV energy range) structure, the center of which approximately corresponds to 240 eV. The magnitude and the energy range of this structure increases with increasing driving frequency. At and above 94.92 MHz, this structure stratifies into two distinct components, with the higher energy of the two components representing the modal  $\text{Ar}^+$  ion energy. The formation of these discrete high-energy peaks represents an increasing fraction of ions exhibiting reduced collisional losses within the sheath volume.

The modal  $\text{Ar}^+$  ion energy exhibits sharp transitions between regions I and II (40.68–54.24 MHz) and II and III (81.36–94.92 MHz),

observed in Figs. 3(d), 3(g), and 3(h). A variation of 280 eV in the modal ion energy  $\hat{\epsilon}_{\text{Ar}^+}$  is achieved over the driving frequency range of 13.56–108.48 MHz. In comparison, the mean ion energy increases in proportion with the driving frequency, varying by 106 eV over the same frequency range. The mean energy exhibits an increased proportionality to the applied voltage amplitude at applied voltage frequencies between 54.24 and 108.36 MHz, correlated with the formation of the structured IEDFs. At 94.92 MHz and above, the modal ion energy exceeds the mean ion energy as it transitions into region III, which increasingly represents the defining region of the IEDF.

## V. MECHANISM FOR THE FORMATION OF STRUCTURED IEDFs

The formation of the structures observed in Figs. 4, 5(g), and 5(h) suggests a reduction in the ion-neutral collision frequency within the sheath. To investigate this, IEDFs incident upon the alumina wall ( $R, Z = 2.1$  mm, 21 mm) for applied-voltage frequencies of 13.56 MHz and 108.48 MHz and applied voltages of 150 V, 300 V, and 450 V are shown in Figs. 5(a) and 5(b). The sheath averaged neutral argon density  $n_{\text{Ar}}$  and the argon ion density  $n_{\text{Ar}^+}$  are shown with respect to the driving frequency in Fig. 5(c), and the associated  $\text{Ar}^+$  mean-free-path  $\lambda_{\text{mfp}}$  and phase-averaged sheath extent  $S_R$  are shown in Fig. 5(d). The  $\text{Ar}^+$  mean-free-path was calculated by employing an Ar- $\text{Ar}^+$  cross section corresponding to the mean  $\text{Ar}^+$  ion velocity at the sheath edge, where the energy resolved cross section was obtained from Ref. 54.

The shape of the IEDFs at 13.56 MHz in Fig. 5(a) is approximately independent of the applied voltage. The variation in the modal  $\text{Ar}^+$  ion energy at this frequency is predominately controlled by the neutral argon density [Fig. 5(c)], which alters the ion-neutral collision rate. Increasing the applied voltage results in an increased maximum ion energy, while the modal energy, denoted by the dashed lines, is not significantly affected ( $1.9 \text{ eV} \leq \hat{\epsilon}_{\text{Ar}^+} \leq 7.7 \text{ eV}$ ). Increasing the applied voltage primarily results in a broadening of the distribution function, resulting in a longer high-energy tail.

In contrast to 13.56 MHz, the shapes of the IEDFs at 108.48 MHz, shown in Fig. 5(b), exhibit a strong dependence on the applied voltage. At 150 V, the IEDF is similar to 13.56 MHz, where the relatively low modal  $\text{Ar}^+$  ion energy ( $\hat{\epsilon}_{\text{Ar}^+} = 9 \text{ eV}$ ) is dictated primarily by the high ion-neutral collision frequency and the majority of distribution is within region I. Increasing the voltage from 150 V to 300 V results in a relatively flat distribution, now predominately within region II, exhibiting an increased modal  $\text{Ar}^+$  ion energy of  $\hat{\epsilon}_{\text{Ar}^+} = 34 \text{ eV}$  and evidence of two additional higher energy structures between 60 and 180 eV. The central and most well defined structure at 108 eV is highlighted in Fig. 5(b) by the red dotted line. At an applied voltage of 450 V, the IEDF consists of three distinct structures, a relatively low-energy peak in region II at 88 eV and two additional higher energy structures in region III at 190 eV and 291 eV, denoted by the blue dotted lines. The modal  $\text{Ar}^+$  ion energy has transitioned from the low-energy region I structure into the highest energy of the two region III structure, and the distribution is now weighted toward the high energy ions as shown in Fig. 4. In this regime, the central energies at which the IEDF structures form are observed to be significantly influenced by the sheath potential via the dc self-bias voltage. The ion-neutral collision frequency within the sheath primarily determines the range of energies within these structures, i.e., their broadening. Note that the dc self-bias voltage  $\phi_{\text{dc}}$  remains approximately constant over

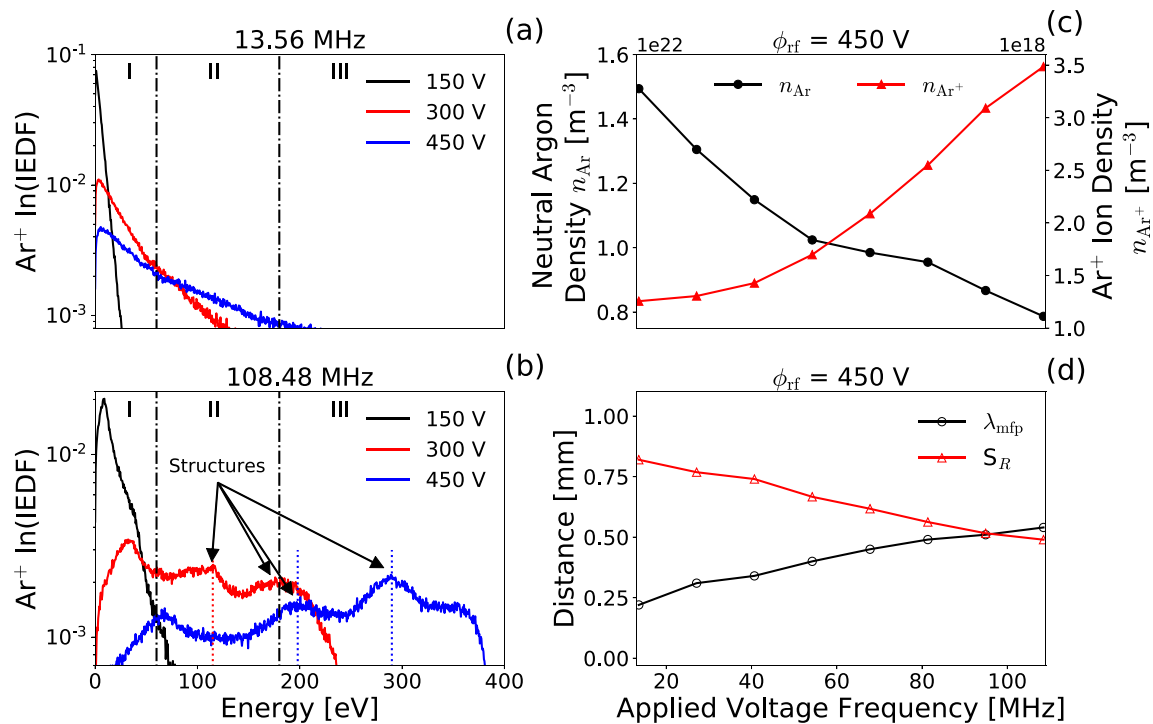


**FIG. 5.**  $\text{Ar}^+$  ion energy distribution functions incident on the dielectric radial wall adjacent to the powered electrode ( $R, Z = 2.1$  mm, 21 mm, see Fig. 1) for applied voltage frequencies of (a) 13.56 MHz and (b) 108.48 MHz and increasing voltage amplitude. Panels (c) and (d) show the effects of varying the driving frequency for a 450 V discharge on the (c) sheath averaged neutral argon  $n_{\text{Ar}}$  and argon ion  $n_{\text{Ar}^+}$  densities and (d)  $\text{Ar}^+$  mean-free-path  $\lambda_{\text{mfp}}$  and phase-averaged sheath extent  $S_R$ . Energy regions I, II, and III are separated by dashed-dotted lines, while IEDF structures are denoted by dotted lines in (a) and (b). The plenum pressure is 200 Pa (1.5 Torr) argon;  $\phi_{\text{rf}} = 150\text{--}450$  V.

the range of driving frequencies employed, varying between  $-303 \text{ V} \leq \phi_{\text{dc}} \leq 282 \text{ V}$  at an applied voltage amplitude of 450 V.

The sheath averaged neutral argon and plasma densities are shown with respect to driving frequency in Fig. 5(c) for an applied voltage of 450 V. Increasing the driving frequency for a fixed applied voltage increases the plasma density and reduces the neutral argon density. The neutral density decreases by approximately 50% from 13.56 MHz to 108.48 MHz. This rarefaction arises from increased neutral gas heating as the deposited power increases with driving frequency. A reduction in the neutral argon density reduces the  $\text{Ar}\text{-}\text{Ar}^+$  collision frequency within the sheath, resulting in an increase in the  $\text{Ar}^+$  mean-free-path, shown in Fig. 5(d). While this increase in the mean-free-path can account for broadening of the IEDFs in Fig. 5(a), it cannot independently account for the narrow and distinct structures observed in Fig. 5(b). To describe the formation of these structures, the properties of the sheath adjacent to the powered electrode, through which ions are accelerated, are considered.

The variation in the phase-averaged sheath extension  $S_R$  with respect to driving frequency is shown in Fig. 5(d). As noted previously, increasing the driving frequency leads to an increased  $\text{Ar}^+$  density adjacent to the powered electrode, giving rise to a reduced sheath width and an increase in the sheath capacitance.<sup>31</sup> The negative dc self-bias voltage at the radial wall enforces an relatively phase-independent radial  $\text{Ar}^+$  ion flux.<sup>31,36,55</sup> A reducing sheath extension coupled with an increasing  $\text{Ar}^+$  mean-free-path results in a reduced chance for ion-neutral collisions within the sheath volume as the

driving frequency increases. Therefore, ion populations that are less influenced by collisions (region II) and effectively collisionless ion populations (region III) may be induced at relatively high (above 94.92 MHz at 1.5 Torr) applied voltage frequencies, enabling a greater degree of control of the range of energies within the IEDF.

## VI. CONCLUSIONS

In conclusion, control of the shape of IEDFs incident on plasma facing material surfaces has been demonstrated via 2D fluid/Monte-Carlo simulations of a radio frequency (13.56–108.48 MHz, 150–450 V) hollow cathode microdischarge operating in argon at 200 Pa (1.5 Torr). Close agreement between simulation and experiment was observed over the range of 13.56–40.68 MHz, and a transition from collisional IEDFs to structured multip peaked IEDFs exhibiting collisionless effects is observed for applied voltage frequencies above 54.24 MHz at 450 V in simulation. Two distinct transitions in the structure of the IEDF are observed at 450 V, corresponding to the formation of a single mid-energy (90–150 eV) structure between 40.68 and 54.24 MHz and two additional high energy ( $\approx 210$  eV,  $\approx 290$  eV) structures which form at frequencies above 81.36 MHz. A significant degree of control of the mean and modal  $\text{Ar}^+$  energies is achieved, varying by 106 eV and 280 eV, respectively. The formation of high energy structures within the IEDFs is attributed to the  $\text{Ar}\text{-}\text{Ar}^+$  mean-free-path increasing beyond the phase-averaged sheath extent as the driving frequency is increased between 13.56 and 108.48 MHz. Supported by self-consistent modeling of the neutral gas temperature,

the increased Ar-Ar<sup>+</sup> mean-free-path is explained by a reduction in the neutral gas density localized to the region adjacent to the powered electrode as a result of gas heating. Inducing structured IEDFs through the application of higher applied voltage frequencies enables enhanced control of the ion-bombardment energy via the applied voltage amplitude under collisional plasma conditions.

## ACKNOWLEDGMENTS

The authors wish to thank M. J. Kushner for provision of the HPEM code and ongoing support, T. Gans and D. O'Connell for fruitful discussions, and P. Hill and R. Armitage for technical support. The work presented herein was funded by the Engineering and Physical Sciences Research Council (EPSRC), Grant No.: EP/m508196/1.

## REFERENCES

- <sup>1</sup>I. Adamovich, S. D. Baalrud, A. Bogaerts, P. J. Bruggeman, M. Cappelli, V. Colombo, U. Czarnetzki, U. Ebert, J. G. Eden, P. Favia, D. B. Graves, S. Hamaguchi, G. Hieftje, M. Hori, I. D. Kaganovich, U. Kortshagen, M. J. Kushner, N. J. Mason, S. Mazouffre, S. M. Thagard, H. R. Metelmann, A. Mizuno, E. Moreau, A. B. Murphy, B. A. Niemira, G. S. Oehrlein, Z. L. Petrovic, L. C. Pitchford, Y. K. Pu, S. Rauf, O. Sakai, S. Samukawa, S. Starikovskaia, J. Tennyson, K. Terashima, M. M. Turner, M. C. Van De Sanden, and A. Vardelle, "The 2017 plasma roadmap: Low temperature plasma science and technology," *J. Phys. D: Appl. Phys.* **50**, 323001 (2017).
- <sup>2</sup>T. Lafleur and J.-P. Booth, "Control of the ion flux and ion energy in CCP discharges using non-sinusoidal voltage waveforms," *J. Phys. D: Appl. Phys.* **45**, 395203 (2012).
- <sup>3</sup>L. Bárdoš, "Radio frequency hollow cathodes for the plasma processing technology," *Surf. Coat. Technol.* **86–87**, 648–656 (1996).
- <sup>4</sup>S. J. Doyle, T. Lafleur, A. R. Gibson, P. Tian, M. J. Kushner, and J. Dedrick, "Enhanced control of the ionization rate in radio-frequency plasmas with structured electrodes via tailored voltage waveforms," *Plasma Sources Sci. Technol.* **26**, 125005 (2017).
- <sup>5</sup>S. Dixon, C. Charles, R. W. Boswell, W. Cox, J. Holland, and R. Gottscho, "Interactions between arrayed hollow cathodes," *J. Phys. D: Appl. Phys.* **46**, 145204 (2013).
- <sup>6</sup>K. J. Kanarik, T. Lill, E. A. Hudson, S. Sriraman, S. Tan, J. Marks, V. Vahedi, and R. A. Gottscho, "Overview of atomic layer etching in the semiconductor industry," *J. Vac. Sci. Technol., A* **33**, 020802 (2015).
- <sup>7</sup>C. Charles, W. Liang, L. Raymond, J. Rivas-Davila, and R. W. Boswell, "Vacuum testing of a miniaturized switch mode amplifier powering an electrothermal plasma micro-thruster," *Front. Phys.* **5**, 36 (2017).
- <sup>8</sup>S. Mazouffre, "Electric propulsion for satellites and spacecraft: Established technologies and novel approaches," *Plasma Sources Sci. Technol.* **25**, 033002 (2016).
- <sup>9</sup>R. A. Arakoni, J. J. Ewing, and M. J. Kushner, "Microdischarges for use as microthrusters: Modelling and scaling," *J. Phys. D: Appl. Phys.* **41**, 105208 (2008).
- <sup>10</sup>D. O'Connell, R. Zorat, A. R. Ellingboe, and M. M. Turner, "Comparison of measurements and particle-in-cell simulations of ion energy distribution functions in a capacitively coupled radio-frequency discharge," *Phys. Plasmas* **14**, 103510 (2007).
- <sup>11</sup>S. Samukawa, M. Hori, S. Rauf, K. Tachibana, P. Bruggeman, G. Kroesen, J. C. Whitehead, A. B. Murphy, A. F. Gutsol, S. Starikovskaia, U. Kortshagen, J.-P. Boeuf, T. J. Sommerer, M. J. Kushner, U. Czarnetzki, and N. Mason, "The 2012 plasma roadmap," *J. Phys. D: Appl. Phys.* **45**, 253001 (2012).
- <sup>12</sup>E. Schüngel, S. Mohr, J. Schulze, U. Czarnetzki, and M. J. Kushner, "Ion distribution functions at the electrodes of capacitively coupled high-pressure hydrogen discharges," *Plasma Sources Sci. Technol.* **23**, 015001 (2013).
- <sup>13</sup>A. Perret, P. Chabert, J. Jolly, and J. P. Booth, "Ion energy uniformity in high-frequency capacitive discharges," *Appl. Phys. Lett.* **86**, 021501 (2005).
- <sup>14</sup>C. Wild and P. Koidl, "Structured ion energy distribution in radio frequency glow-discharge systems," *Appl. Phys. Lett.* **54**, 505–507 (1989).
- <sup>15</sup>J. Liu, G. L. Huppert, and H. H. Sawin, "Ion bombardment in rf plasmas," *J. Appl. Phys.* **68**, 3916–3934 (1990).
- <sup>16</sup>A. Manenschijn, G. C. Janssen, E. Van Der Drift, and S. Radelaar, "Measurement of ion impact energy and ion flux at the rf electrode of a parallel plate reactive ion etcher," *J. Appl. Phys.* **69**, 1253–1262 (1991).
- <sup>17</sup>C. Wild and P. Koidl, "Ion and electron dynamics in the sheath of radio-frequency glow discharges," *J. Appl. Phys.* **69**, 2909–2922 (1991).
- <sup>18</sup>W. C. Chen, X. M. Zhu, S. Zhang, and Y. K. Pu, "Reconstruction of ion energy distribution function in a capacitive rf discharge," *Appl. Phys. Lett.* **94**, 211503 (2009).
- <sup>19</sup>S. Sharma, A. Sen, N. Sirse, M. M. Turner, and A. R. Ellingboe, "Plasma density and ion energy control via driving frequency and applied voltage in a collisionless capacitively coupled plasma discharge," *Phys. Plasmas* **25**, 080705 (2018).
- <sup>20</sup>J. T. Gudmundsson, D. I. Snorrason, and H. Hannesdottir, "The effect of pressure and driving frequency on electron heating in a capacitively coupled oxygen discharge," *Plasma Sources Sci. Technol.* **27**, 025009 (2018).
- <sup>21</sup>A. Agarwal, S. Rauf, and K. Collins, "Gas heating mechanisms in capacitively coupled plasmas," *Plasma Sources Sci. Technol.* **21**, 055012 (2012).
- <sup>22</sup>S. J. Doyle, R. Gibson, J. Flatt, T. S. Ho, R. W. Boswell, C. Charles, P. Tian, M. J. Kushner, and J. Dedrick, "Spatio-temporal plasma heating mechanisms in a radio-frequency electrothermal microthruster," *Plasma Sources Sci. Technol.* **27**, 085011 (2018).
- <sup>23</sup>C. Charles and R. W. Boswell, "Measurement and modelling of a radio-frequency micro-thruster," *Plasma Sources Sci. Technol.* **21**, 022002 (2012).
- <sup>24</sup>C. Charles, J. Dedrick, R. W. Boswell, D. O'Connell, and T. Gans, "Nanosecond optical imaging spectroscopy of an electrothermal radiofrequency plasma thruster plume," *Appl. Phys. Lett.* **103**, 124103 (2013).
- <sup>25</sup>A. Greig, C. Charles, N. Paulin, and R. W. Boswell, "Volume and surface propellant heating in an electrothermal radio-frequency plasma micro-thruster," *Appl. Phys. Lett.* **105**, 054102 (2014).
- <sup>26</sup>A. Greig, C. Charles, and R. W. Boswell, "Simulation of main plasma parameters of a cylindrical asymmetric capacitively coupled plasma micro-thruster using computational fluid dynamics," *Front. Phys.* **2**, 80 (2015).
- <sup>27</sup>T. S. Ho, C. Charles, and R. W. Boswell, "A comprehensive cold gas performance study of the pocket rocket radiofrequency electrothermal micro-thruster," *Front. Phys.* **4**, 55 (2017).
- <sup>28</sup>T. S. Ho, C. Charles, and R. W. Boswell, "Neutral gas heating and ion transport in a constricted plasma flow," *Phys. Plasmas* **24**, 084501 (2017).
- <sup>29</sup>T. S. Ho, C. Charles, and R. W. Boswell, "Performance modelling of plasma microthruster nozzles in vacuum," *J. Appl. Phys.* **123**, 173301 (2018).
- <sup>30</sup>M. A. Lieberman and A. J. Lichtenberg, *Principles of Plasma Discharges and Materials Processing*, 2nd ed. (John Wiley & Sons, New Jersey, 2005), pp. 403, 434–441.
- <sup>31</sup>M. Lieberman, "Analytical solution for capacitive RF sheath," *IEEE Trans. Plasma Sci.* **16**, 638–644 (1988).
- <sup>32</sup>C. Charles, R. Hawkins, and R. W. Boswell, "Particle in cell simulation of a radiofrequency plasma jet expanding in vacuum," *Appl. Phys. Lett.* **106**, 093502 (2015).
- <sup>33</sup>T. Lafleur and R. W. Boswell, "Particle-in-cell simulations of hollow cathode enhanced capacitively coupled radio frequency discharges," *Phys. Plasmas* **19**, 023508 (2012).
- <sup>34</sup>A. Derzi, I. Korolov, E. Schüngel, Z. Donkó, and J. Schulze, "Effects of fast atoms and energy-dependent secondary electron emission yields in PIC/MCC simulations of capacitively coupled plasmas," *Plasma Sources Sci. Technol.* **24**, 034002 (2015).
- <sup>35</sup>M. J. Kushner, "Hybrid modelling of low temperature plasmas for fundamental investigations and equipment design," *J. Phys. D: Appl. Phys.* **42**, 194013 (2009).
- <sup>36</sup>S. J. Doyle, A. R. Gibson, R. W. Boswell, C. Charles, and J. P. Dedrick, "Control of electron, ion and neutral heating in a radio-frequency electrothermal micro-thruster via dual-frequency voltage waveforms," *Plasma Sources Sci. Technol.* **28**, 035019 (2019).
- <sup>37</sup>A. Salabaş and R. P. Brinkmann, "Non-neutral/quasi-neutral plasma edge definition for discharge models: A numerical example for dual frequency hydrogen capacitively coupled plasmas," *Jpn. J. Appl. Phys., Part 1* **45**, 5203–5206 (2006).



- <sup>38</sup>P. Tian and M. J. Kushner, "Controlling VUV photon fluxes in low-pressure inductively coupled plasmas," *Plasma Sources Sci. Technol.* **24**, 34017 (2015).
- <sup>39</sup>M. Hayashi, Technical Report No. IPPJ-AM-19, Nagoya Institute of Technology, 1991.
- <sup>40</sup>K. Tachibana, "Excitation of the  $1s_5$ ,  $1s_4$ ,  $1s_3$  and  $1s_2$  levels of argon by low-energy electrons," *Phys. Rev. A* **34**, 1007 (1986).
- <sup>41</sup>D. Rapp and P. EnglanderGolden, "Total cross sections for ionization and attachment in gases by electron impact. I. Positive ionization," *J. Chem. Phys.* **43**, 1464–1479 (1965).
- <sup>42</sup>N. A. Dyatko, Y. Z. Ionikh, I. V. Kochetov, D. L. Marinov, A. V. Meshchanov, A. P. Napartovich, F. B. Petrov, and S. A. Starostin, "Experimental and theoretical study of the transition between diffuse and contracted," *J. Phys. D: Appl. Phys.* **41**, 055204 (2008).
- <sup>43</sup>A. Bogaerts, R. G. V. Serikov, and V. V. Serikov, "Calculation of gas heating in direct current argon glow discharges," *J. Appl. Phys.* **87**, 8334 (2000).
- <sup>44</sup>H. W. Ellis, R. Y. Pai, E. W. McDaniel, E. A. Mason, and L. A. Viehland, "Transport properties of gaseous ions over a wide energy range," *At. Data Nucl. Data Tables* **17**, 177–210 (1976).
- <sup>45</sup>T. Gans, C. C. Lin, V. S.-v. der Gathen, and H. F. Döbele, "Phase-resolved emission spectroscopy of a hydrogen rf discharge for the determination of quenching coefficients," *Phys. Rev. A* **67**, 12707 (2003).
- <sup>46</sup>T. Gans, D. O'Connell, V. Schulz-von der Gathen, and J. Waskoenig, "The challenge of revealing and tailoring the dynamics of radio-frequency plasmas," *Plasma Sources Sci. Technol.* **19**, 034010 (2010).
- <sup>47</sup>S. Siepa and U. Czarnetzki, "Line integration and spatial resolution in optical imaging of plasmas," *J. Phys. D: Appl. Phys.* **48**, 385201 (2015).
- <sup>48</sup>J. Schulze, Z. Donkó, B. G. Heil, D. Luggenhölscher, T. Mussenbrock, R. P. Brinkmann, and U. Czarnetzki, "Electric field reversals in the sheath region of capacitively coupled radio frequency discharges at different pressures," *J. Phys. D: Appl. Phys.* **41**, 105214 (2008).
- <sup>49</sup>A. V. Phelps and Z. L. Petrovic, "Cold-cathode discharges and breakdown in argon: Surface and gas phase production of secondary electrons," *Plasma Sources Sci. Technol.* **8**, R21–R44 (1999).
- <sup>50</sup>J. Schulze, E. Schüngel, Z. Donkó, D. Luggenhölscher, and U. Czarnetzki, "Phase resolved optical emission spectroscopy: A non-intrusive diagnostic to study electron dynamics in capacitively radio frequency discharges," *J. Phys. D: Appl. Phys.* **43**, 124016 (2010).
- <sup>51</sup>J. Schulze, Z. Donkó, T. Lafleur, S. Wilczek, and R. P. Brinkmann, "Spatio-temporal analysis of the electron power absorption in electropositive capacitive RF plasmas based on moments of the Boltzmann equation," *Plasma Sources Sci. Technol.* **27**, 055010 (2018).
- <sup>52</sup>A. R. Gibson, Z. Donkó, L. Alelyani, L. Bischoff, G. Hübner, J. Bredin, S. J. Doyle, I. Korolov, K. Niemi, T. Mussenbrock, P. Hartmann, J. P. Dedrick, J. Schulze, T. Gans, and D. O'Connell, "Disrupting the spatio-temporal symmetry of the electron dynamics in atmospheric pressure plasmas by voltage waveform tailoring," *Plasma Sources Sci. Technol.* **28**, 01LT01 (2019).
- <sup>53</sup>V. Godyak, R. Piejak, and B. Alexandrovich, "Measurements of electron energy distribution in low-pressure R F discharges," *Plasma Sources Sci. Technol.* **1**, 36–58 (1992).
- <sup>54</sup>A. V. Phelps, "The application of scattering cross sections to ion flux models in discharge sheaths," *J. Appl. Phys.* **76**, 747–753 (1994).
- <sup>55</sup>M. J. Kushner, "Distribution of ion energies incident on electrodes in capacitively coupled rf discharges," *J. Appl. Phys.* **58**, 4024–4031 (1985).